Entanglement of Conjugated Polymer Chains Influences Molecular Self-Assembly and Carrier Transport

*Kui Zhao, Hadayat Ullah Khan, Ruipeng Li, Yisong Su, and Aram Amassian**

The influence of polymer entanglement on the self-assembly, molecular packing structure, and microstructure of low-M_w (lightly entangled) and high-M_w (highly entangled) poly (3-hexylthiophene) (P3HT), and the carrier transport in thin-film transistors, are investigated. The polymer chains are gradually disentangled in a marginal solvent via ultrasonication of the polymer solution, and demonstrate improved diffusivity of precursor species (coils, aggregates, and microcrystallites), enhanced nucleation and crystallization of P3HT in solution, and self-assembly of well-ordered and highly textured fibrils at the solid–liquid interface. In low-M_w P3HT, reducing chain entanglement enhances interchain and intrachain ordering, but reduces the interconnectivity of ordered domains (tie molecules) due to the presence of short chains, thus deteriorating carrier transport even in the face of improving crystallinity. Reducing chain entanglement in high-M_w P3HT solutions increases carrier mobility up to ≈20-fold, by enhancing interchain and intrachain ordering while maintaining a sufficiently large number of tie molecules between ordered domains. These results indicate that charge carrier mobility is strongly governed by the balancing of intrachain and interchain ordering, on the one hand, and interconnectivity of ordered domains, on the other hand. In high-M_w P3HT, intrachain and interchain ordering appear to be the key bottlenecks to charge transport, whereas in low-M_w P3HT, the limited interconnectivity of the ordered domains acts as the primary bottleneck to charge transport.

1. Introduction

Conjugated polymers have garnered significant interest in recent years as they promise to enable solution-printed, large-area, low-cost, and flexible electronics and photovoltaics.[1–9] Studies of structure-performance relationships in conjugated polymer-based organic thin-film transistors (OTFTs) have revealed that charge carrier transport in polymer semiconductors is mediated by crystallinity, molecular orientation, and by intergrain connectivity.[10–12] Conjugated polymers such as poly(3-hexylthiophene) (P3HT)[13–15] are thought to be difficult to push into a highly crystalline state, owing to chain entanglement which hinders molecular diffusion and requires challenging conformational transitions of the semi-flexible backbone and the flexible side-chains.[16,17] These intrinsic characteristics have therefore limited polymer semiconductors from reaching their full performance potential and has so far put them at a disadvantage in some respects when compared to highly crystalline conjugated small molecules. To overcome these limitations, intensive attempts have been made to improve the crystalline order in polymers such as P3HT based on the belief that crystallinity is a crucial requirement for fast charge transport, for instance, by thermal annealing,[18,19] by strain-aligning,[20] by mixing solvents,[21] and by treating the surface of the substrate,[10,22] among other methods. All of the above strategies have been shown to yield marginal improvements in mobility and have been consistently attributed to a higher degree of crystalline order observed in the polymer thin films.

In considering the limited response of conjugated polymer thin films to the above processing knobs and stimuli, one can see that the intrinsic characteristics of polymers are crucial mediators and bottlenecks of their solid-state structure and performance. Typically, phase transition from coil-like molecules to a crystal exhibiting long range order consists of complex nucleation and growth processes.[24] The nucleation process, independent of whether it is occurring in the melt or in a dilute/concentrated solution, implies conformational changes of the polymer chain from coil-like chains to rod-like lamellae, with strong implications on the extent and size of the resulting lamellae.[25–28] Previous investigations of P3HT crystallization have revealed the rod-stacking step as the rate-limiting process, since the associated free energy of formation (ΔG = 37.5 kcal mol^{-1}) is larger than the free energy of activation of the coil-to-rod transformation (ΔF = 23.7 kcal mol^{-1}).[29] The attachment of polymer molecules at the growth front is also a complex process, involving polymer diffusion, entanglement effects, backbone torsion, and competitive attachment/detachment at the growth front in the presence of solvent, among other mechanistic steps.[24] The influence of entanglement, which has been investigated in great detail for flexible polymers,[30,31] is much less discussed for conjugated polymers with semi-flexible backbone and long and flexible side-chains, despite its great importance to π-stacking

Dr. K. Zhao, Dr. H. U. Khan. Dr. R. Li, Y. Su,
Prof. A. Amassian
Materials Science and Engineering
Division of Physical Sciences and Engineering
King Abdullah University of Science and Technology (KAUST)
Thuwal, Saudi Arabia
E-mail: aram.amassian@kaust.edu.sa

DOI: 10.1002/adfm.201301007

© 2013 WILEY-VCH Verlag GmbH & Co. KGaA, Weinheim

in conjugated polymers. The most successful description of entangled networks of semi-flexible polymers in this realm is the famous "tube model" pioneered by de Gennes[32] and by Doi and Edwards.[33] According to this model, entanglement is mainly controlled by chain tortuosity. The more tortuous the chains are, the more entanglement junctions there will be, and the lesser the chains can diffuse and slip during deformation under applied stress.[34] For semi-flexible conjugated polymers, the interference from entanglement decreases the diffusivity of the chains and increases the overall viscosity of the solution.[35,36] Chains are thus trapped and hindered from forming anything other than a disordered or a semi-ordered structure; this is understandably more predominant in the case of long polymer chains than in shorter ones, and mediates their molecular weight (M_w)-dependent properties, including charge transport.[37,38] Importantly, the main drawback of chain entanglement, which is to hinder crystalline ordering, is mitigated by the fact that long chains are likely to participate in the formation of several crystalline domains at once, thus allowing long chains to bridge crystalline domains with so-called tie molecules, thus improving the electrical interconnectivity of different parts of the polymer film.[37,39] This suggests there is an important chain length-entanglement structure-performance relationship to be explored, and highlights the importance of understanding and developing means of tuning entanglement and chain interconnectivity both in solution- and in solid-states, to achieve faster carrier transport through polymer thin films.

Ultrasonication has been known to disentangle flexible polymer chains[40] by facilitating the free movement of chains, and more recently has been used successfully to enhance the lamellar and π–π^* crystallinity of conjugated polymer thin films.[41,42] In a previous report by Aiyar et al.,[42] enhanced crystallinity resulting from ultrasonication was credited with increasing the carrier mobility of P3HT (M_w = 47.7 kDa) thin films. In this study, we tune the degree of entanglement in low- and high-M_w P3HT solutions using ultrasonication, and demonstrate that crystallinity is not always the answer to enhancing carrier transport in polymer films. Disentanglement of short and long polymer chains, both, improves intrachain conjugation length, interchain interactions, and overall crystallinity. However, the carrier mobility of low-M_w P3HT (M_w = 35 kDa) OTFTs decreases slightly, while dramatic improvements are measured in high-M_w P3HT (M_w = 68 kDa) OTFTs. In the case of low-M_w P3HT, charge transport between crystalline regions appears to be the bottleneck, as it relies mainly on interchain hopping in the absence of tie molecules connecting adjacent crystalline regions. In high-M_w P3HT, ordered domains are well interconnected via intrachain transport through tie molecules. As such, the main bottlenecks to transport in high-M_w P3HT appear to be interchain and intrachain transport within ordered regions, which are greatly improved by reducing chain entanglement.

2. Results and Discussion

2.1. Chain Length, Conformation, and Entanglement

P3HT chains are well represented by an "alternating inverse comb".[43] In poor solvents, solvophobic effects drive coil-like chains to adopt a rod-like behavior.[44] However, whichever conformation the P3HT chain adopts, entanglement always exists and obstructs the chains from adopting a highly-ordered structure.[35,45,46] The presence of entanglement depends strongly upon polymer molecular weight, because of the latter's effect on chain contour length and tortuosity.[45] The average molecular chain contour length, L_{chain},[39,47] is expressed as $L_{\text{chain}} = l_0 M_w/(M_0 B)$, l_0 = 3.8 Å for a unit of 3-hexylthiophene,[47] M_0 = 168.3 g mol^{-1}, and B is a coefficient whose value is 2.0 for conjugated molecules.[48] We estimate L_{chain} ≈39 nm for low-M_w P3HT chains and ≈77 nm for high-M_w P3HT chains, respectively. The width of P3HT fibrils, also known as the lamellar thickness, was previously reported to range between 15 nm and 30 nm for a broad range of molecular weights investigated.[12,39] This is so, because if chain length is much larger than ≈20–30 nm,[12,39] the chains behave moreso like a flexible polymer with chain folding and distortion, as illustrated in **Figure 1**a, than as a rigid rod. The tortuosity of long chains favors the binary-hooking geometry seen in Figure 1b,[34,49,50] which acts as an entanglement. The comparatively short chains in low-M_w P3HT do not lend themselves to significant chain folding, instead adopting an extended conformation and plain contacts (Figure 1c,d). As most of the chains are 20–30 nm in length, they can form single-hooks, but the small tortuosity of the chains means that entanglement is fewer in these samples than in high-M_w ones.

The number of chain entanglement in solution state, N, can be estimated using:[51]

$$N = \frac{M_w}{M_e^{\text{solution}}} \approx \frac{2M_w}{M_c^{\text{solution}}} \tag{1}$$

Here, M_e^{solution} is the entanglement molar mass and M_c^{solution} is the molecular weight at which entanglement begins to influence the macroscopic properties of the solution, such as viscosity. It is estimated that $M_e^{\text{solution}} \sim 2M_c^{\text{solution}}$.[51] The viscosity of a 0.1 wt% P3HT solution in chlorobenzene (21 °C) was found to exhibit a sharp upturn when $M_w \geq M_c^{\text{solution}}$ ≈35 kDa.[52] The conditions of the present study are different; namely, toluene is a marginal solvent for P3HT in comparison to chlorobenzene, a good solvent; the concentration investigated in the mentioned work is five times more dilute. These differences indicate that the solutions investigated in this study should be comparatively more entangled. Nevertheless, we use this to make a conservative and coarse estimation of the relative number of entanglements in the low- and high-M_w solutions and find N ≈1–2 for the low-M_w P3HT and N ≈4 for the high-M_w P3HT used in this study.

2.2. Disentangling Polymer Chains

While chain entanglement cannot be observed directly, its effects are readily detectable by monitoring polymer aggregation and crystallization in the presence of solvophobic forces, or by evaluating the comparative diffusivity of polymer chains and associated precursors in the solution, as will be presented in Section 2.6. Room temperature UV–Vis absorption spectra of pristine and ultrasonicated solutions of high- and low-M_w P3HT are presented in **Figures 2**a,b, respectively.

© 2013 WILEY-VCH Verlag GmbH & Co. KGaA, Weinheim

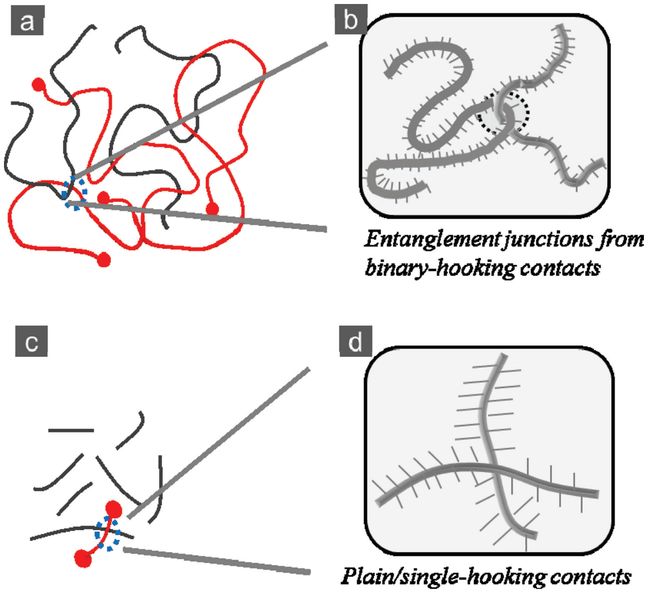

Figure 1. Schematic model showing molecular conformation and entanglement in high- and low-M_w P3HT. a) The randomly stacked long chains with folding and distortion of conformation of high-M_w polymer. b) Entanglement junctions formed from binary-hooking contacts of long chains. c) The randomly dispersed short chains with extended conformation of low-M_w polymer. d) Plain or single-hooking contacts from short chains, unable to form significant entanglement.

We report only on the spectral range from 500 to 700 nm, where intrachain and interchain absorption peaks are active, as shorter wavelengths are blocked by the non-diluted solution. For high-M_w P3HT solutions, disentanglement via ultrasonication leads to dramatically increased absorption at both ≈560 nm and ≈616 nm, indicating strong *J*- and *H*-photophysical aggregation, suggestive of microcrystallite formation in the solution.[42,44] Low-M_w solutions are also responsive to disentanglement, but the effect is far less dramatic due to entropic effects, which increase the solubility of short chains and remove the solvophobic driving force.[41,53] The relative concentration of microcrystallites (Figure 2c) is calculated using Lambert-Beer's law (Table S1, Supporting Information). The microcrystallite concentration is found to increase 18-fold for the high-M_w polymer solution but only 1.7-fold for the low-M_w one. This indicates that a significant fraction of polymer chains (those transformed into crystallites) can no longer participate in chain entanglement in the solution state. The intrachain absorption peaks of high-M_w P3HT solution exhibit a slight blue-shift from ≈616 to ≈611 nm upon ultrasonication. The high-M_w solution was further investigated by dynamic light scattering (DLS) to determine the trend in *Z*-average size of P3HT aggregates and polydispersity index (PDI) (Figure S2, Supporting Information, and Figure 2d). We observe a gradual decrease of aggregate size from ≈208 to ≈98 nm with treatment time, while the PDI decreases from 0.55 to 0.38. Both the UV-Vis and DLS data indicate a dramatically increased density of smaller nuclei sporting a much narrower size distribution.

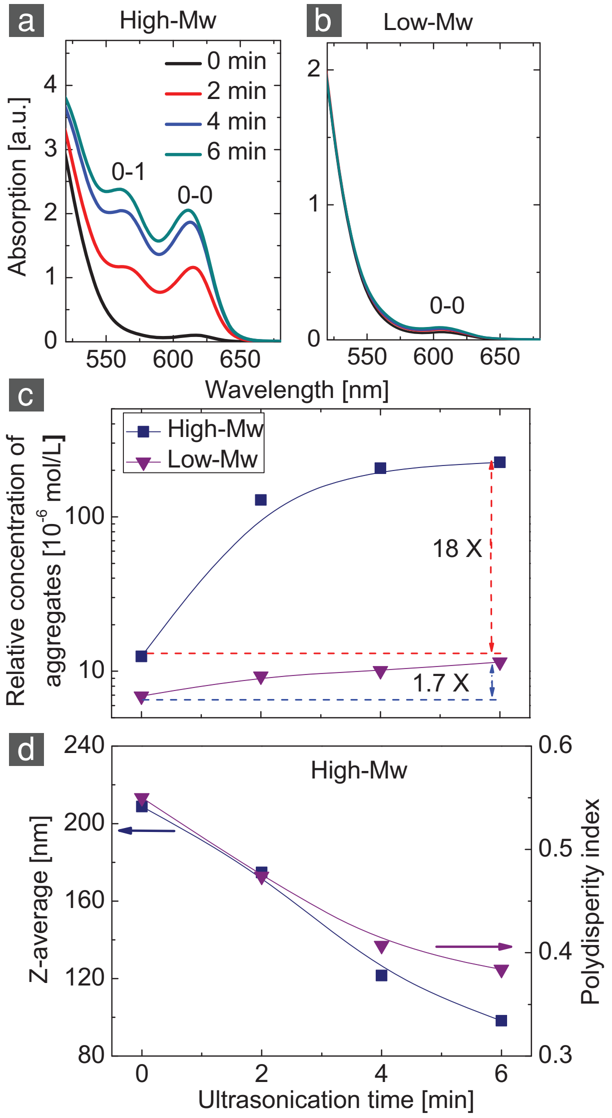

Figure 2. Precursor state of high- and low-M_w P3HT in a toluene solution. Static UV-Vis absorption spectra of a) high-M_w and b) low-M_w P3HT solutions in toluene with increasing ultrasonication time at room temperature. c) Concentration of π-stacked P3HT in solution calculated by applying the Lambert-Beer's law to the absorption peak located at 610 nm for both high-M_w and low-M_w solutions. d) *Z*-average size and polydispersity index estimated for high-M_w P3HT aggregates from DLS measurements. UV-Vis absorption measurements are performed on actual solutions (0.5 wt%), whereas DLS measurements are performed on 10-times diluted solutions (0.05 wt%).

2.3. Entanglement and Photophysical Aggregates

Quantitative analysis of intrachain and interchain interactions in spin-cast P3HT thin films is performed by means of static absorption spectroscopy and quantitative modeling. The absorbance spectra of high-M_w P3HT thin films from various solution states are shown in **Figures 3**a and Figure S3, Supporting Information. The absorption spectrum is composed of two parts, a crystalline part due to photophysically

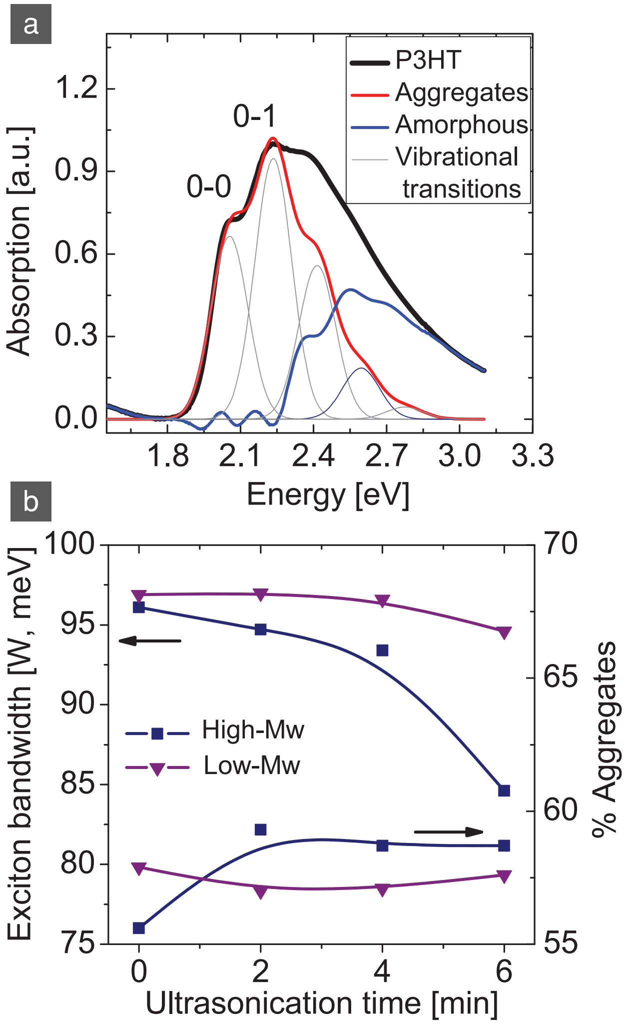

Figure 3. a) Absorption spectrum of a high-M_w P3HT thin film subjected to the Spano analysis using Equation 2. b) The evolution of exciton bandwidth W (left axis) and percentage of film made up of aggregates (right axis) with ultrasonication time for low- and high-M_w samples.

interacting chains and monomers, and an amorphous contribution due to disordered chains. Equation 2, based on weakly interacting H-aggregates in polythiophenes, was used to separate the absorption contributions of photophysical aggregates and amorphous P3HT regions and to analyze the former:[11,54]

$$\mathrm{A}(E) \propto \sum_{m=0} \left(\frac{S^m}{m!}\right) \times \left(1 - \frac{We^{-s}}{2E_\mathrm{p}} \sum\nolimits_{n\neq m} \frac{S^n}{n!n - (m)}\right)^2 \times \exp\left(\frac{(E - E_{0-0} - \mathrm{m}E_\mathrm{p} - 1/2\, WS^m e^{-S})^2}{2\sigma^2}\right) \tag{2}$$

Here, A is the absorbance as a function of the photon energy (E), W is the free exciton bandwidth of the aggregates, S is the Huang-Rhys factor and fixed at a value of 1.0 taken from a Franck-Condon fit,[55] m and n are differing vibrational levels, $E_{0\text{-}0}$ is the 0–0 transition energy, E_p is the intermolecular vibrational energy and taken as 0.18 eV,[56] and σ is the Gaussian linewidth. W is inversely related to the width of the cofacially packed chain segments in P3HT aggregates, and gradually decreases from ≈96 meV to ≈84 meV with ultrasonication time for high-M_w thin films and from ≈97 meV to ≈95 meV for low-M_w P3HT (**Figure 3**b). The decrease by ≈12 meV/≈2 meV for high-/low-M_w P3HT indicates a positive effect of disentanglement on intrachain order, with far more improvement observed for long chains as compared to short chains. The number of interacting thiophene repeat units (M) can be estimated from the relationship between exciton bandwidth and number of repeat units found from the simulations of Gierschner et al.[57] Graphical interpolation suggests a marginal increase of the number of interacting repeat units for high-M_w P3HT from ≈37 to ≈43 for pristine and ultrasonicated solutions. No change is seen in the case of low-M_w P3HT (Figure S3c, Supporting Information). The increasing conjugation length is a rough estimate and will be compared with direct lamellar thickness measurements in Section 2.7.

The fraction of P3HT molecules involved in the aggregated state was also deduced. The aggregation was found to be ≈55% in pristine, high-M_w thin films, and increased to ≈59% by ultrasonicating the solution. By contrast, the low-M_w sample shows greater aggregation from the start and remains nearly constant at (57.5 ± 0.5)%, indicating the low-M_w films crystallize more easily than high-M_w films.

2.4. Crystallization and Microstructure

In **Figure 4**a, we plot the lamellar diffraction intensity (area under the (100) Bragg peak) for high- and low-M_w thin films obtained from grazing incidence X-ray diffraction (GIXRD) measurements. The thickness-corrected intensity (raw diffraction data and film thickness are shown in the Supporting Information, Figures S4,S5, separately) reveals the high-M_w P3HT exhibits a saturated crystallinity window for ultrasonicated samples, which peaks at a 1.6-fold larger value as compared to the untreated film. By contrast, the lamellar crystallinity of low-M_w samples increases only marginally.

The spacing along the lamellar stacking direction calculated from GIXRD before and after treatment decreases slightly for high-M_w films, but increases slightly for low-M_w films (Figure 4b). The correlation length associated to lamellar ordering is calculated from GIXRD using the Debye-Scherrer method. We find it to range from 13.5 to 15.5 nm for high-M_w samples, and from 13.5 to 14.1 nm for the low-M_w samples. However, as there are no contributions of electronic coupling along the lamellar stacking direction due to the presence of side-chains,[58] the overlap or tilt between side-chains from neighboring lamellae[59] should not directly affect charge carrier hopping along the π-stacking direction, unless if it improves the crystallinity in that direction as well.

The π-stacking behavior was investigated by plan-view TEM and selected area electron diffraction (ED). The π-stacking ring (020) was clearly observed for all the samples indicative of molecular “edge-on” orientation (Figure S6, Supporting Information).[60,61] The (020) peak intensity obtained from normalized spectra increases significantly with treatment time for

© 2013 WILEY-VCH Verlag GmbH & Co. KGaA, Weinheim

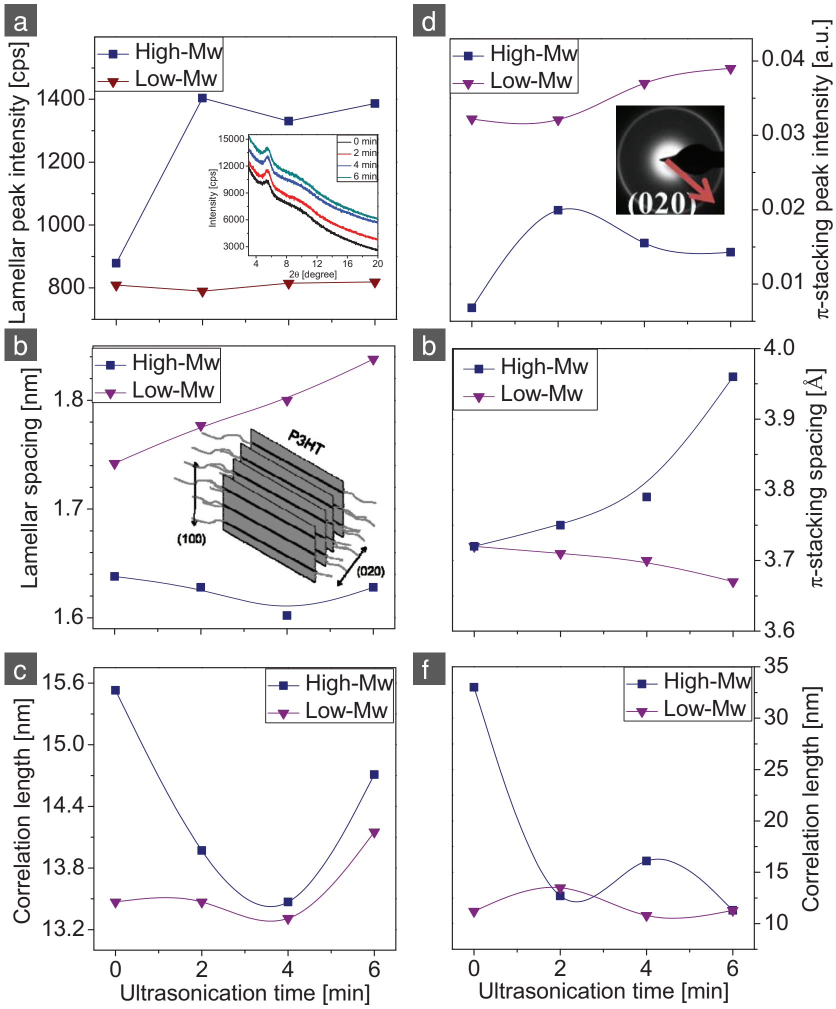

Figure 4. Microstructure of low- and high-M_w P3HT in thin films prepared from solutions with various precursor states. a) The (100) Bragg peak intensity normalized to film thickness from GIXRD showing variation of lamellar stacking crystallinity. b) The out-of-plane spacing of lamellar stacking calculated from GIXRD data. c) Correlation length corresponding to the lamellar stacking along the [100] direction calculated by Debye-Scherrer analysis from GIXRD data. d) The (020) peak intensity from electron diffraction profile normalized to film thickness showing variation of π-stacking crystallinity. e) The in-plane π-stacking spacing calculated from electron diffraction. f) Correlation length corresponding to the in-plane π-stacking direction calculated by Debye-Scherrer analysis from electron diffraction.

high-M_w samples and only slightly for low-M_w samples. A gradual increase of the π–π^* separation of high-M_w P3HT with increased treatment time from 3.72 Å to 3.96 Å is consistent with the slight blue-shift in the interchain absorption peak in solution. Only a marginal change is seen in case of low-M_w P3HT. The correlation length along the π-stacking direction[62] was also calculated from ED and is shown in Figure 4f. For high-M_w samples, the correlation length decreases from ≈33 nm down to ≈11–16 nm, whereas low-M_w samples exhibit little or no change. The increases in lamellar and (020) diffraction intensities and simultaneous decrease of the correlation length in the lamellar and π-stacking directions might suggest the formation of a much larger number of smaller/shorter fibrils in high-M_w thin-films. In contrast, the low-M_w films exhibit a marginal increase of crystallinity in the lamellar and π-stacking directions, indicating a slight increase of the number density of low-M_w crystallites.

Both GIXRD and ED results are consistent with decreasing fibril length and lamellar stacking in the solid state, while the number of fibrils increases significantly in the solid state. The lamellar thickness changes as well, as will be discussed in Section 2.7.

2.5. Texture and Molecular Orientation in Thin Films

The anisotropic chain-packing was investigated by variable angle spectroscopic ellipsometry (VASE) performed over a large range of incidence angles.[63,64] The ordinary (electric-field vector parallel to the plane of the surface) and extra-ordinary (out-of-plane or perpendicular) refractive indices (n_o and n_e) and extinction coefficients (k_o and k_e) are shown in **Figure 5**a. As expected, k_o is much larger than k_e, since both *H*- and *J*-aggregates form in the plane of the substrate. $k_{o(0\text{-}0)}$ (at 2.05 eV) and $k_{o(0\text{-}1)}$ (at 2.25 eV)—designated as interchain and intrachain interactions, respectively—increase with ultrasonication time in the case of high-M_w samples (Figure 5b), indicating increased π–π^* interactions in the plane of the substrate. By contrast, the low-M_w sample exhibits smaller values of k which do not vary appreciably with ultrasonication time, in agreement with UV-Vis absorption and ED analyses.

The anisotropy of the film can be estimated by calculating the birefringence (see Figure 5c), $\Delta n = n_o - n_e$. Δn depends upon ultrasonication time, increasing strongly for high-M_w samples, while decreasing slightly for low-M_w films. The increase of Δn implies higher anisotropy of chain-packing in both crystalline and amorphous regions of P3HT. To verify this trend in the case of ordered domains, we perform grazing incidence wide angle X-ray scattering (GIWAXS) measurements. The azimuthal full width at half maximum (FWHM) of the (100) Bragg sheet is used to estimate the lamellar orientation distribution (see Figure 5e).[10,64,65] The FWHM decreases from 19.7° to 14.8° with increasing ultrasonication time for high-M_w samples (Figure 5f), whereas the same treatment leaves the FWHM of low-M_w films nearly unchanged. This indicates that optical anisotropy can be largely explained by changes in lamellar texture.

2.6. Molecular Diffusion and Self-Assembly

Molecular diffusivity is a critical factor for promoting crystallization and self-assembly in the presence of solvophobic effects

© 2013 WILEY-VCH Verlag GmbH & Co. KGaA, Weinheim

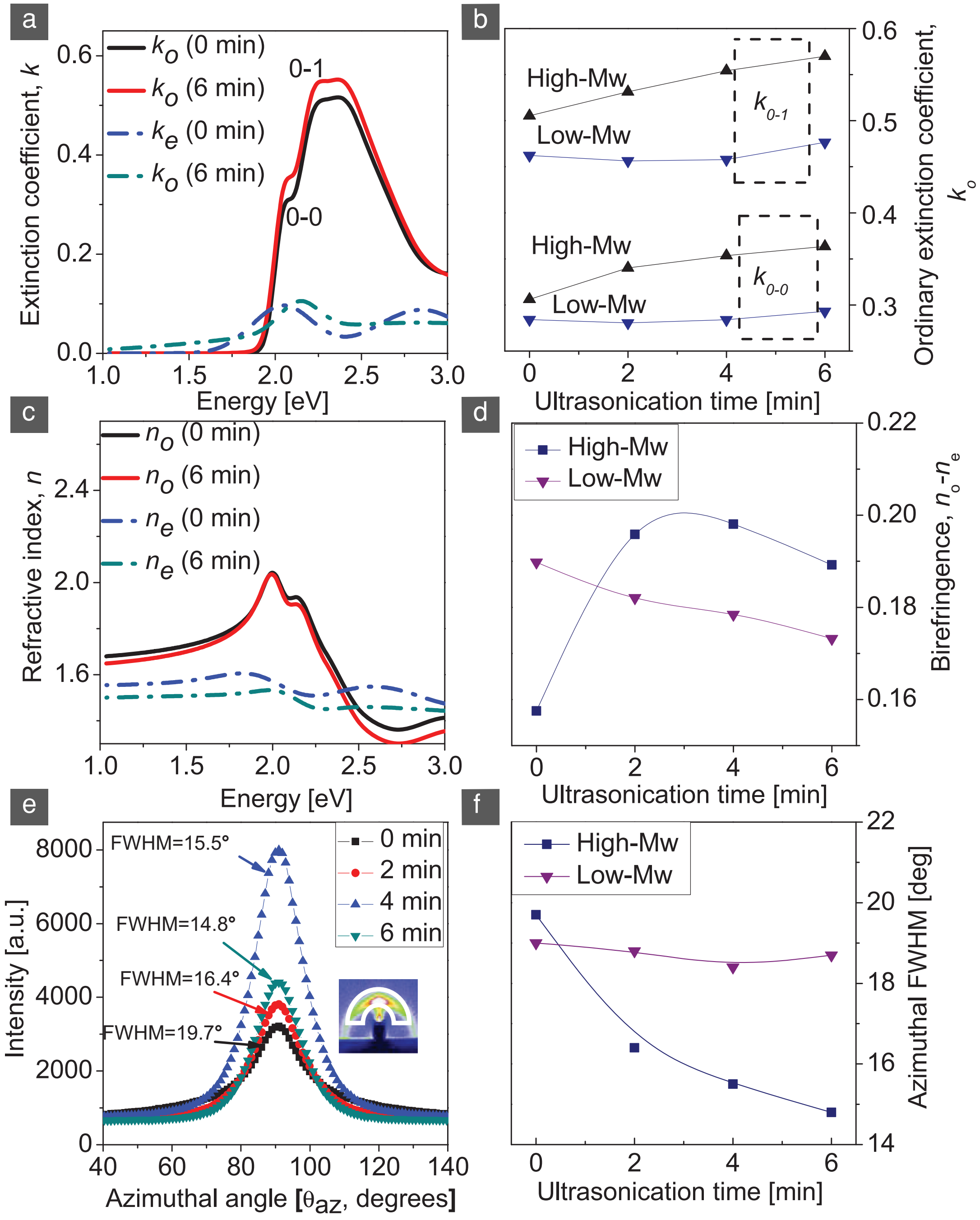

Figure 5. The anisotropic chain-packing in low- and high-M_w thin films investigated by VASE and GIWAXS. a) The ordinary and extraordinary extinction coefficients (k_o and k_e, respectively) obtained from VASE showing electronic coupling preferentially in the plane of the substrate. b) The evolution of the ordinary extinction coefficient $k_{o(0\text{-}0)}$ (at 2.05 eV) and $k_{o(0\text{-}1)}$ (at 2.25 eV) with ultrasonication time for low- and high-M_w samples. c) The ordinary and extra-ordinary refractive indices (n_o and n_e, respectively) obtained from VASE showing birefringence of chains-packing. d) The evolution of birefringence ($n_o - n_e$) at transparent region 1.55 eV with ultrasonication time for low- and high-M_w samples. e) The full width half maximum (FWHM) of the azimuthal-angle intensity of the q_z = (100) peaks from GIWAXS. f) The evolution of azimuthal FWHM with ultrasonication time for low- and high-M_w samples.

and/or during drying of the solution. To gauge this qualitatively, a 95 µL drop of toluene was dispensed upon the surface of a substrate, as shown in **Figure 6**a. Upon stabilization of the drop, a small, 5 µL drop of P3HT solution was dispensed over the solvent. As the solute mixes with and diffuses into the bulk solvent, we monitor the spread of the solute visually as indicated by the expansion of the dark solution into the clear solvent, as seen by the colorful circles drawn in Figure 6b. The

© 2013 WILEY-VCH Verlag GmbH & Co. KGaA, Weinheim

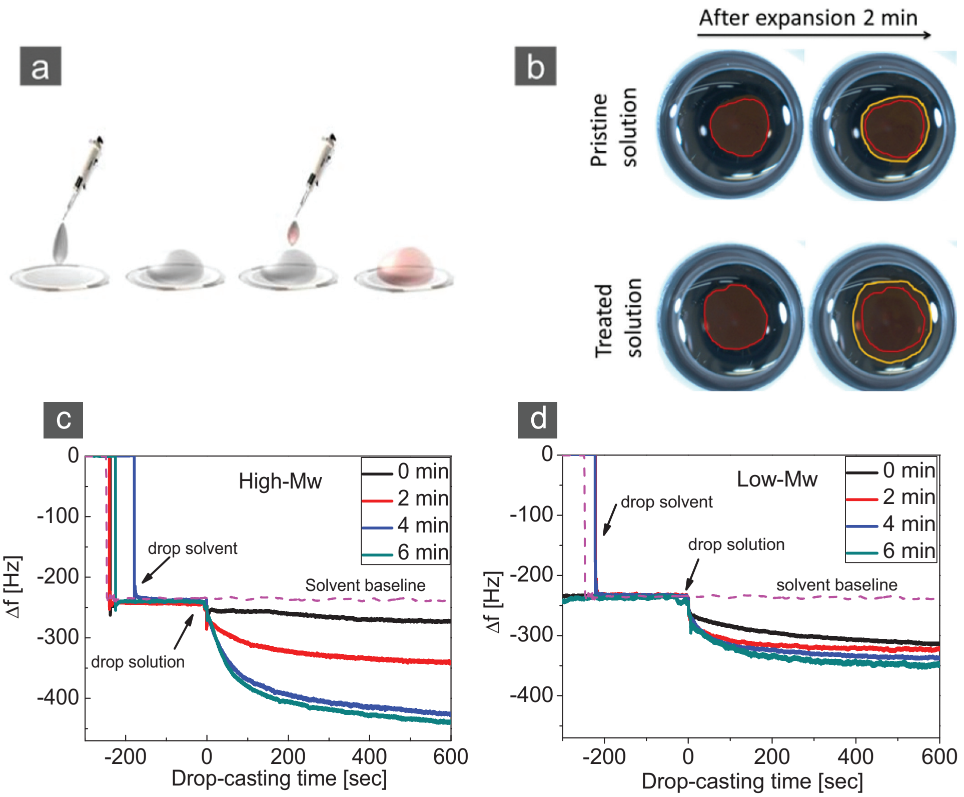

Figure 6. Molecular diffusion in high- and low-M_w P3HT solutions measured by QCM-D. a) Schematic representation showing the drop-casting of 5 µL of the treated solution onto a SiO_2-terminated quartz sensor covered with 95 µL of toluene. b) Images of P3HT solution spreading into toluene for pristine solution and ultrasonicated solution immediately and two minutes after drop-casting. Representative QCM-D results for c) high-M_w P3HT and d) low-M_w solutions with different precursor states, respectively.

untreated high-M_w solute remains stuck in place, whereas the treated solution spreads out more rapidly. This difference is ascribed to increased freedom for molecular and aggregate movement/diffusion as reduced chain entanglement induced by ultrasonicating the solution in the presence of solvophobic forces drives crystallization of polymer chains and reduces the concentration of dissolved polymer chains at the expense of polymer crystallites and aggregates in solution.

We have utilized solution quartz crystal microbalance with dissipation (QCM-D) capability (a technique recently employed in organic electronics)[66,67] to investigate how the diffusing solute self-assembles at the surface of the SiO_2-coated quartz sensor. The shear waves produced by the oscillating quartz crystal do not propagate in the solution due to the impedance mismatch between the crystal and the liquid medium. An evanescent wave is thus formed and decays within ≈200–300 nm from the surface of the sensor, making it sensitive only to changes in the mass and the viscoelastic properties of the material bound at the solid–liquid interface. In Figures 6c,d, we plot ΔF with respect to drop-casting of high- and low-M_w solutions treated for different times. We detect significant decrease of the resonance frequency of the sensor upon casting the solution, indicating that the diffusing solute attaches to the surface of the sensor. Stabilization of ΔF indicates attachment–detachment processes occur at equal rates. As expected, we find that entanglement also affects the self-assembly of P3HT at the solid–liquid interface. The increased deposition mass could be ascribed to increased nucleation rate on substrate on one hand and the precipitation of large crystallites on the other hand. As chains tend to nucleate at the solid–liquid interface forming an buried interfacial layer,[68] we suspect that the increased mobility and diffusivity of species helps to accelerate the nucleation rate at the solid–liquid interface and achieves improved lamellar texture, as demonstrated above. Meanwhile, we know that disentanglement in the presence of solvophobic forces[69] leads to formation of more microcrystallites in high-M_w P3HT than in low-M_w P3HT due to differences in the solubility of short and long polymer chains and consequently upon differences in the solubility of low-M_w crystallites versus high-M_w crystallites. As the solvophobic effect driving solidification is the same in all samples, we explain the increased deposition rate and equilibrium mass as being due to increased molecular diffusivity, reduced solubility of P3HT microcrystallites in toluene, and significantly increased abundance of free-floating microcrystallites.

2.7. Thin-Film Microstructure and Morphology

Spin-coating is a very fast process which, at first, ejects the bulk of the solution, and subsequently kinetically traps the polymer film by rapidly drying the solution in a matter of seconds.[70] Hence, increasing the diffusivity and crystallization kinetics at

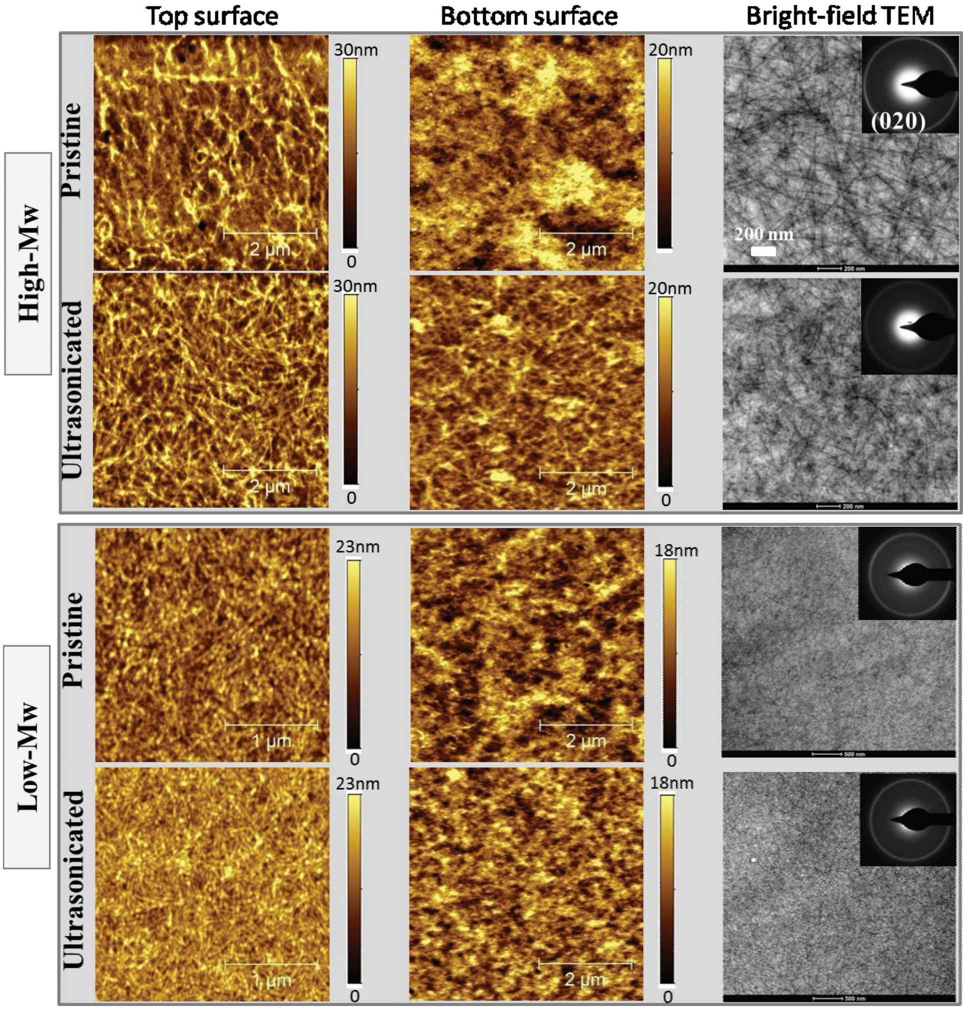

Figure 7. Thin-film morphology for high- and low-M_w P3HT samples prepared from pristine and 6 min ultrasonicated solutions. The top-surface (left) and bottom-surface (intermediate) of thin films investigated by AFM show increased number of high-M_w P3HT fibrils and a smoother semiconductor–dielectric interface. The bulk morphology of thin films is revealed by plan-view bright-field TEM (right), indicating increased number of shorter fibrils. The lamellar thickness was measured for various samples as a function of ultrasonication time (Figure S7, Supporting Information). The inset of electron diffraction (ED) shows the (020) diffraction ring.

room temperature can lead to the formation of comparatively more ordered films within the same process duration. We have utilized atomic force microscopy (AFM) and transmission electron microscopy (TEM) to evaluate the microstructure and surface/interface morphology of the thin films, as shown in **Figure 7** and Figure S6, Supporting Information. Films obtained from highly entangled high-M_w solutions exhibit long, noodle- or spaghetti-like features with many twists, and bends on the top surface and appear to show nondescript features at the bottom surface of the film, that is, at the semiconductor–dielectric interface. Thin films of ultrasonicated high-M_w P3HT form uniformly distributed and closely packed fibrillar features with a shorter length and with fibrils now clearly visible near the bottom surface of the film, indicating these may increasingly take part in charge carrier transport.

The evolution of lamellar thickness is a key microstructural feature related to backbone extension[12] and is predicted to increase with chain disentanglement. TEM inspection indeed reveals lamellar thickness (fibril width) to increase from ≈14.9 nm to ≈17.7 nm, ≈18.9 nm, and 19.3 nm with ultrasonication times of 0, 2, 4, and 6 min, respectively, as shown in Figure S7, Supporting Information. The observation of extended chain backbone is consistent with increased intrachain conjugation length in *J* aggregates as indicated by the reduced exciton bandwidth reported in Figure 3b, and believed to improve carrier transport within the aggregates.[59,60] In comparison, films prepared from low-M_w P3HT exhibit considerably finer fibrils, making it difficult to measure their dimensions from current TEM images.

2.8. Carrier Transport and Discussion

Bottom-gate, top-contact OTFTs were fabricated by spin-coating the pristine and ultrasonicated solutions of high- and low-M_w P3HT onto clean SiO_2. The average field-effect,

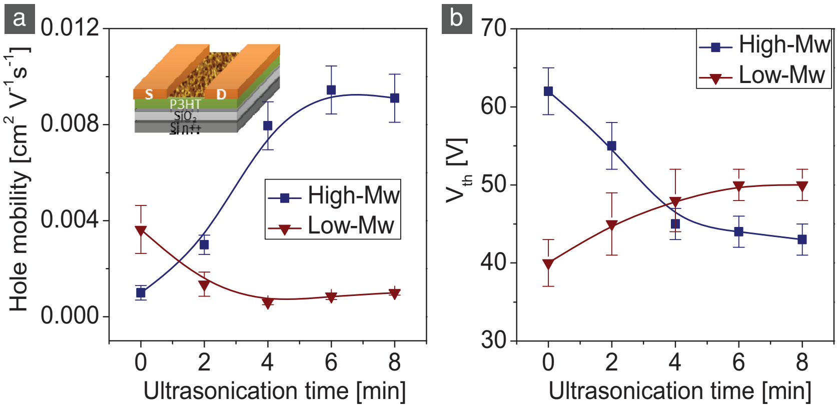

Figure 8. Carrier transport in top-contact P3HT OTFTs. a) Hole mobilities for low- and high-M_w P3HT OTFTs are shown against ultrasonication time ranging from 0 to 8 min. The mean mobility and error bars are calculated from a minimum of 4 devices. b) V_{th} vs ultrasonication time graph for both low and high-M_w P3HT devices. The error bars are the V_{th} variation from minimum of four devices at each ultrasonication time. The detailed transfer and output characteristics as well as threshold voltage are shown in the Supporting Information, Figure S8. All devices were fabricated and measured as-deposited in ambient conditions.

saturation hole mobility is extracted from the transfer curves (Figure S8a–c, Supporting Information) and plotted in **Figure** 8a. The mobility improves nearly 20-fold (i.e., from ≈0.0005 to ≈0.0105 cm^2 V^{-1} s^{-1}) upon ultrasonication-induced disentanglement of high-M_w P3HT for a duration of 4 min, then saturates for 6 and 8 min treatment times. Meanwhile, for low-M_w P3HT the starting mobility is better than pristine high-M_w films, that is, 0.005 cm^2 V^{-1} s^{-1}, but has a five-fold decrease with ultrasonication. Ultrasonication also affects the threshold voltage (V_{th}) of the devices. As the ultrasonication time increases from 0 to 4 min, the V_{th} decreases from 62 to 45 V (Figure 8b) for high-M_w films, and increases from 40 to 50 V in case of low-M_w films.

The enhanced charge transport in high-M_w P3HT thin films prepared from ultrasonicated solutions highlights the intricate dependence of transport properties upon molecular self-assembly and chain entanglement. Disentanglement promotes segmental chain motion, facilitates conformational transition in the presence of solvophobic force, and shortens the time for chains to rearrange at the growth front. The crystallization in solution is seen to increase dramatically as a result (**Figure** 9a). The 18-fold increase in π–π absorption and decrease of the average diameter of P3HT aggregates by half suggests the nucleation density of such crystallites increases dramatically. This reduces the fraction of polymer chains in solution and the overall entanglement in the solution, consequently enhancing molecular diffusivity and facilitating self-assembly of more ordered P3HT at the semiconductor-dielectric interface (Figure 9b).

Charge transport in polymer OTFTs is determined by the slowest process. Transport within the domains is assured by a combination of intrachain and interchain processes, whereas transport between domains relies on a combination of domain boundary hopping and the presence or not of tie molecules linking ordered domains via intrachain transport. The mixed responses of OTFT performance to clear improvements of crystallinity via disentanglement in cases of low- and high-M_w polymers makes it clear that carrier transport is not determined by crystallinity of P3HT alone, but also by the presence of tie molecules linking ordered domains as shown in Figure 9c. Domain boundary hopping does not appear to be an efficient process, as demonstrated by the poor performance response of low-M_w P3HT even in the face of improved crystallinity, intrachain and interchain interactions, and visibly greater presence of ordered fibrils at the semiconductor–dielectric interface. This is most likely due to the passage of charges from one ordered domain to another through crystalline-amorphous boundaries without well-defined molecular conformation and packing.[71,72] This makes it clear that interdomain transport is the main bottleneck in case of low-M_w P3HT.

By contrast, intradomain transport via tie molecules seems to greatly assist transport in long-chain P3HT. Disentanglement of high-M_w P3HT chains led to drastic increase in the nucleation density of crystallites in solution as well as a marked reduction of fibrillar length in the solid state; yet, carrier transport improved 20-fold as tie molecules appear to be highly effective at carrying charges, indicating that intradomain transport is the real bottleneck to charge transport in high-M_w P3HT. Improved carrier mobility with increasing crystallinity, improved intrachain backbone planarity and stronger in-plane interchain interactions further support this point. This is probably why high-M_w P3HT generally yields higher carrier mobility, are responsive to thermal or solvent vapor annealing, and is often more desirable for OTFTs.[37,59]

3. Conclusions

We investigated the influence of polymer entanglement in terms of the chain length-entanglement-structure-performance relationship using both high- and low-M_w P3HT. Polymer chains were gradually disentangled in a marginal solvent via ultrasonication of the polymer solution, resulting in improved diffusivity of precursor species, enhanced formation of microcrystallites in solution, and enhancement of interchain and intrachain interactions in thin films via formation of highly textured fibers near the semiconductor–dielectric interface. The field-effect mobility decreases five-fold in low-M_w P3HT thin films, whereas dramatic improvement of ≈20-fold is measured in the case of high-M_w P3HT. Such differences can be understood to stem from differences in the mechanism of carrier transport in low- and high-M_w P3HT. In low-M_w P3HT, short chains have few entanglements and very few tie molecules. As such, domain boundaries act as bottleneck to charge transport. In the case of high-M_w P3HT, disentanglement of the polymer chain improves interchain and intrachain interactions and promotes carrier transport, indicating that intradomain transport is the main bottleneck due to the large number of chain entanglement. These results indicate that charge carrier mobility is strongly governed by the balancing of intrachain and interchain

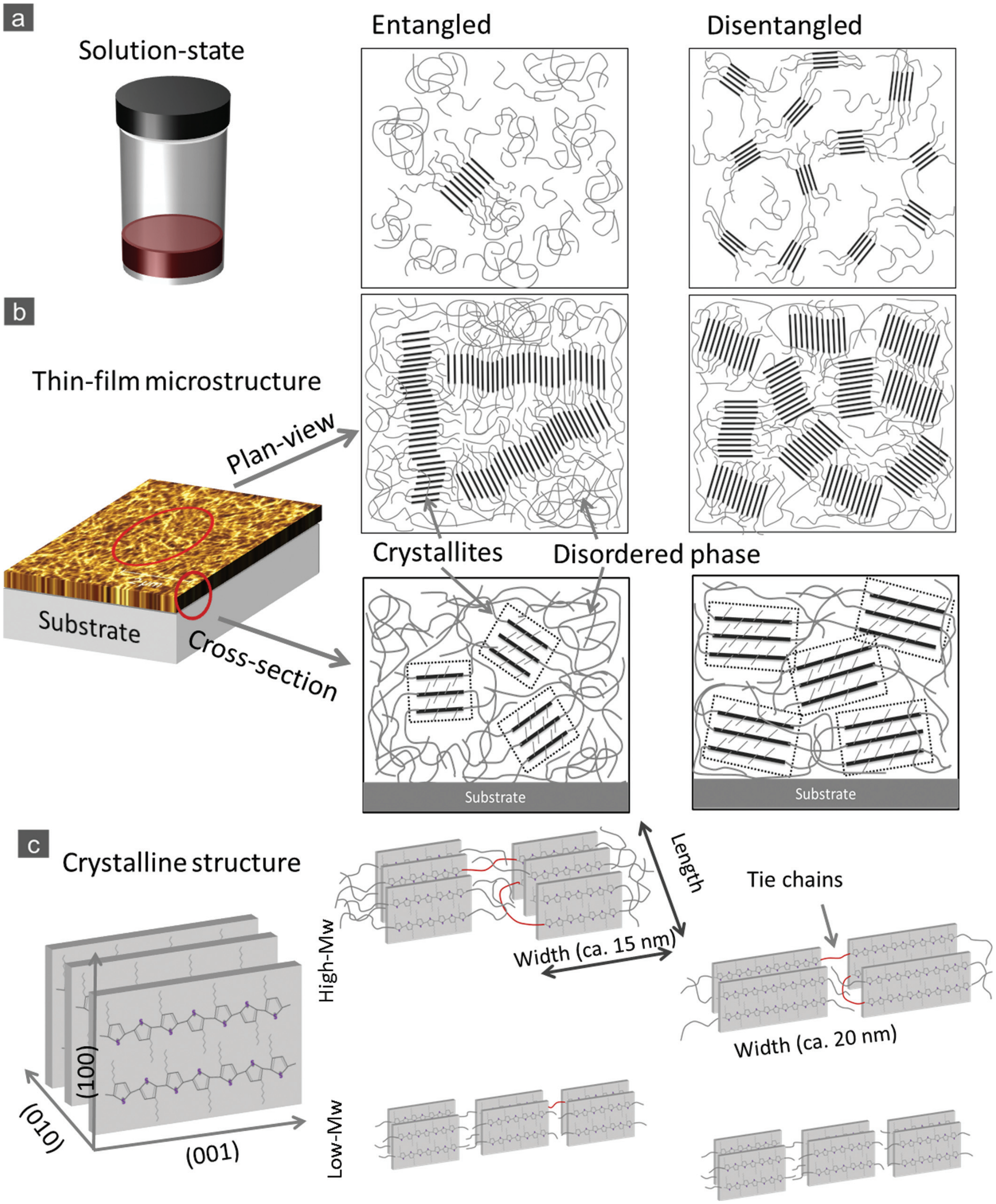

Figure 9. Schematic model of how molecules self-assemble in the entangled (pristine) and disentangled systems. a) The solution-state of high-M_w P3HT indicating entanglement giving rise to a small number of microcrystallites owing to reduced diffusivity and conformational change; disentanglement resulting from ultrasonicated solutions results in the formation of a large number of microcrystallites and nuclei, exhibiting increased diffusivity and uniform size distribution. b) The microstructure of the solid-state films showing, in the case of entangled systems, reduced molecular self-assembly with fewer crystalline domains, large mosaicity, and rough semiconductor–dielectric (S–D) interface. In case of disentangled chains, well-ordered and highly textured fibrils are formed throughout the film, resulting in improved mosaicity and enhanced crystallinity near the S–D interface. c) The crystalline structure of P3HT films shows different molecular packing behavior for both high- and low-M_w polymers when the system is disentangled. For high-M_w polymers, disentanglement decreases fibrillar length [010] and fibril height (lamellar stacking direction) [100], increases lamellar thickness (fibril width) [001], and improves overall intrachain and interchain interactions, while maintaining a sufficiently large number of tie molecules (red chains) between ordered domains. With respect to low-M_w polymers, disentanglement breaks up the few ties existing between different crystalline regions, resulting in reduced interdomain transport.

© 2013 WILEY-VCH Verlag GmbH & Co. KGaA, Weinheim

ordering on the one hand and interconnectivity of ordered domains on the other hand.

4. Experimental Section

Materials: Regioregular P3HT (catalog no. 445703 and 698989) and toluene (anhydrous, 99.8%) were purchased from Sigma Aldrich and used without further purification. The P3HT used in this study had M_w of 68 kDa (high-M_w) and 35 kDa (low-M_w) as determined by gel permeation chromatography (GPC).

Solution Preparation: P3HT was dissolved in toluene (0.5 wt%) at elevated temperature 60 °C for 10 min and then kept stirring in dark environment over two days at room temperature. The obtained solution was ultrasonicated at room temperature for 0, 2, 4, 6, and 8 min. Ultrasonication was performed by using a Bransonic cleaner (model 1510E-DTH) with frequency of 42 kHz. The solutions were placed in small glass vials and were placed in the basin of the ultrasonic bath. The flow fields created by ultrasonication result in chain disentanglement while maintaining the same polymer chemical properties as demonstrated by GPC measurements performed before and after ultrasonication on both low- and high-M_w P3HT (Figure S9a–d, Supporting Information).

Device Fabrication and Characterization: Highly doped n-type silicon wafers (100) with thermally evaporated 300 nm SiO_2 were used for bottom-gate OTFT fabrication. Initially, the substrates were cleaned by rinsing with acetone, isopropanol, ethanol, and Milli Q, followed by Standard Clean 1 (RCA) ammonium hydroxide (30% NH_4OH), hydrogen peroxide (30% H_2O_2), and de-ionized water (with 1:1:5 ratio) for 15 min at 70 °C. Substrates were blown dry with N_2. After heating at 100 °C for 10 min, the substrates were treated with UV-ozone for 10 min. Solutions of P3HT were spin-cast onto substrates at a speed of 1000 rpm for 30 s. Gold source–drain electrodes were evaporated through a shadow mask with a channel width *(W)* of 500 µm and length *(L)* of 30 µm. All electrical measurements were performed with a Keitheley 4200 Semiconductor Characterization System in ambient air.

Variable Angle Spectroscopic Ellipsometry: VASE was performed using a M-2000XI rotating compensator (J. A. Woollam Co., Inc) to determine the thickness and the optical properties of the spin-cast films on Si (100) with a 300 nm thermal oxide. VASE spectra ranging from 210 nm to 1689 nm were recorded at 18 different angles of incidence with respect to the substrate normal from 45° to 79°, with 2° increment. In the manuscript, a spectral range from 400 nm to 800 nm is displayed. Optical analysis of VASE data was performed using the EASE and WVASE32 software packages (J. A. Woollam Co., Inc). Optical modeling was performed assuming a homogeneous thin film exhibiting uniaxial anisotropy.

UV-Vis Absorption: Spectra were acquired on a Cary 5000 (Varian) instrument. P3HT solution was filled in a 0.5 mm-thick quartz cuvette.

Dynamical Light Scattering: DLS was carried out using Zetasizer Nano ZS system from Malvern Instruments Ltd. at room temperature. For the instruments detection range, the 0.5 wt% solution was diluted to 0.05 wt%.

Gel Permeation Chromatography: GPC was performed by using a triple detection size exclusion chromatography system comprised of a DAWN HELEOS multi-angle light scattering (MALS) detector (Wyatt Technology Corporation, Santa Barbara, USA), a Viscostar viscometer (Wyatt Technology Corporation, Santa Barbara, USA), and an Optilab-rEX refractive index detector (RID) (Wyatt Technology Corporation, Santa Barbara, USA). Tetrahydrofuran (THF) solvent was used to dissolve the pristine polymer as well as the dried polymer from the ultrasonicated toluene solution separately. 100 µL of each sample were injected for analysis. Since the polymer is colored, data was collected with and without Forward Monitor correction enabled in the MALS detector. Data Analysis was performed using the Astra software (Wyatt Technology Corporation, Santa Barbara, USA). No significant difference was observed between data sets of the the untreated and treated polymer, indicating the polymer chains were not damaged by ultrasonication.

Self-Assembly of P3HT Characterization: A quartz crystal microbalance with dissipation capability (QCM-D, model E4, Q-sense, Biolin Scientific) was used with quartz sensors coated with silicon dioxide (200 nm) to characterize the self-assembly of P3HT at the solid–liquid interface. A drop of 95 µL toluene solvent was cast into a closed chamber and kept in equilibrium for 2 min, followed by a 5 µL drop of solution. All measurements were performed at 20 °C. Changes in frequency of the fifth overtone ($n = 5$) are presented herein.

Transmission Electron Microscopy: TEM experiments were carried out on a FEI Tecnai 12 operated at 120 kV accelerating voltage. Samples for TEM were prepared by floating the thin film in water and picking it up using a 300 mesh copper grid. The surface analysis for the samples was carried out by AFM "Agilent 5400 SPM".

Grazing Incidence Wide Angle X-Ray Scattering: GIWAXS measurements were carried out at D-line at the Cornell High Energy Synchrotron Source (CHESS) at Cornell University. A 0.5 × 0.1 mm beam size with a wavelength of 1.23 Å and wide band pass (1.47%) was generated from double-bounce multilayer monochromator. The incidence angle was 0.15° with respect to the substrate plane, as established by performing X-ray reflectivity using an ion chamber. A 50 × 50 mm charged coupling device (CCD) area detector (Medoptics) with pixel size of 46.9 µm was placed at a distance of 92 mm from the sample stage. A 1.5 mm-wide tantalum rod was used to block the intense scattering at low angles of incidence.

Grazing Incidence X-Ray Diffraction: GIXRD measurements were carried out in a scanning interval of 2θ between 3° and 20° on Bruker D8 Discover with X-ray wavelength of 1.54 Å. We employed an incident angle ($\theta = 0.2°$) slightly above the critical angle ($\theta = 0.18°$).

Supporting Information

Supporting Information is available from the Wiley Online Library or from the author.

Acknowledgements

The authors would like to thank Dr. Detlef-M. Smilgies for help with acquisition of GIWAXS data at CHESS, Prof. Yu Han for help with acquisition of UV-Vis spectra at KAUST, and Dr. Misjudeen Raji for help with GPC experiments at KAUST. The authors acknowledge Prof. Carlos Silva, Dr. Natalie Stingelin, Prof. Alberto Salleo, and Dr. Neil Treat for helpful discussions. Part of this work was supported by KAUST's Office of Competitive Research Funds under FIC and AEA awards.

Received: March 21, 2013
Revised: May 28, 2013
Published online: June 26, 2013

---

[1] A. C. Arias, J. D. MacKenzie, I. McCulloch, J. Rivnay, A. Salleo, *Chem. Rev.* **2010**, *110*, 3.
[2] R. H. Friend, R. W. Gymer, A. B. Holmes, J. H. Burroughes, R. N. Marks, C. Taliani, D. D. C. Bradley, D. A. D. Santos, J. L. Bredas, M. Logdlund, W. R. Salaneck, *Nature* **1999**, *397*, 121.
[3] D. Wohrle, D. Meissner, *Adv. Mater.* **1991**, *3*, 129.
[4] M. Ikawa, T. Yamada, H. Matsui, H. Minemawari, J. Tsutsumi, Y. Horii, M. Chikamatsu, R. Azumi, R. Kumai, T. Hasegaw, *Nat. Commun.* **2012**, *3*, 1176.
[5] Z. B. Henson, K. Müllen, G. C. Bazan, *Nat. Chem.* **2012**, *4*, 699.
[6] H. Sirringhaus, M. Ando, *MRS Bull.* **2008**, *33*, 676.
[7] B. K. Yap, R. Xia, M. Campoy-Quiles, P. N. Stavrinou, D. D. C. Bradley, *Nat. Mater.* **2008**, *7*, 376.
[8] U. T. Yamamoto, K. Takimiya, H. Kuwabara, M. Ikeda, T. Sekitani, T. Someya, H. Klauk, *Adv. Mater.* **2011**, *23*, 654.

© 2013 WILEY-VCH Verlag GmbH & Co. KGaA, Weinheim

[9] K. Zhao, G. Zhou, Q. Wang, Y. Han, L. Wang, D. Ma, *Macromol. Chem. Phys.* **2010**, *211*, 313.
[10] R. J. Kline, M. D. McGehee, M. F. Toney, *Nat. Mater.* **2006**, *5*, 222.
[11] P. Pingel, A. Zen, R. D. Abellón, F. C. Grozema, L. D. A. Siebbeles, D. Neher, *Adv. Funct. Mater.* **2010**, *20*, 2286.
[12] R. Zhang, B. Li, M. C. Iovu, M. Jeffries-EL, G. Sauvé, J. Cooper, S. Jia, S. Tristram-Nagle, D. M. Smilgies, D. N. Lambeth, R. D. McCullough, T. Kowalewski, *J. Am. Chem. Soc.* **2006**, *128*, 3480.
[13] G. Horowitz, M. E. Hajlaoui, R. Hajlaoui, *J. Appl. Phys.* **2000**, *87*, 4456.
[14] Z. Bao, A. Dodabalapur, A. J. Lovinger, *Appl. Phys. Lett.* **1996**, *69*, 4108.
[15] T.-A. Chen, X. Wu, R. D. Rieke, *J. Am. Chem. Soc.* **1995**, *117*, 233.
[16] R. D. Mccullough, *Adv. Mater.* **1998**, *10*, 93.
[17] I. Mcculloch, M. Heeney, M. L. Chabinyc, D. Delongchamp, R. J. Kline, M. Coelle, W. Duffy, D. Fischer, D. Gundlach, B. Hamadani, R. Hamilton, L. Richter, A. Salleo, M. Shkunov, D. Sporrowe, S. Tierney, W. Zhong, *Adv. Mater.* **2009**, *21*, 1091.
[18] S. Cho, K. Lee, J. Yuen, G. Wang, D. Moses, A. J. Heeger, M. Surin, R. Lazzaroni, *J. Appl. Phys.* **2006**, *100*, 114503.
[19] D. Choi, S. Jin, Y. Lee, S. H. Kim, D. S. Chung, K. Hong, C. Yang, J. Jung, J. K. Kim, M. Ree, C. E. Park, *ACS Appl. Mater. Interfaces* **2010**, *2*, 48.
[20] B. O'Connor, R. J. Kline, B. R. Conrad, L. J. Richter, D. Gundlach, M. F. Toney, D. M. DeLongchamp, *Adv. Funct. Mater.* **2011**, *21*, 3697.
[21] D. H. Kim, Y. Jang, Y. D. Park, K. Cho, *J. Phys. Chem. B* **2006**, *110*, 15763.
[22] A. Salleo, M. L. Chabinyc, M. S. Yang, R. A. Street, *Appl. Phys. Lett.* **2002**, *81*, 4383.
[23] J. F. Chang, J. Clark, N. Zhao, H. Sirringhaus, D. W. Breiby, J. W. Andreasen, M. M. Nielsen, M. Giles, M. Heeney, I. McCulloch, *Phys. Rev. B* **2006**, *74*, 115318.
[24] M. Muthukumar, *Adv. Chem. Phys.* **2004**, *128*, 1.
[25] J. I. Lauritzen, J. D. Hoffman, *J. Res. Nat. Bur. Std.* **1960**, *64A*, 73.
[26] E. A. DiMarzio, *J. Chem. Phys.* **1967**, *47*, 3451.
[27] G. Allegra, *J. Chem. Phys.* **1977**, *66*, 5453.
[28] E. Passaglio, E. A. DiMarzio, *J. Chem. Phys.* **1987**, *87*, 1539.
[29] S. Malik, T. Jana, A. K. Nandi, *Macromolecules* **2001**, *34*, 275.
[30] J. Klein, *Macromolecules* **1978**, *11*, 852.
[31] R. P. Wool, *Macromolecules* **1993**, *26*, 1564.
[32] P. G. de Gennes, *Scaling Concepts in Polymer Physics*, Cornell University Press, IthacaNY, **1979**.
[33] M. Doi, S. F. Edwards, *The Theory of Polymer Dynamics*, Clarendon Press, Oxford, **1986**.
[34] S. Wu, *J. Polym. Sci., Polym. Phys.* **1989**, *27*, 723.
[35] S. M. Aharoni, *Macromolecules* **1983**, *16*, 1722.
[36] I. Bitsanis, H. T. Davis, M. Tirrell, *Macromolecules* **1988**, *21*, 2824.
[37] R. J. Kline, M. D. McGehee, E. N. Kadnikova, J. S. Liu, J. M. J. Frechet, *Adv. Mater.* **2003**, *15*, 1519.
[38] S. Joshi, *PhD Thesis*, Siegen University, Germany **2008**.
[39] M. Brinkmann, P. Rannou, *Macromolecules* **2009**, *42*, 1125.
[40] Y. Chen, H. Li, *J. Polym. Sci., Part B: Polym. Phys.* **2007**, *45*, 1226.
[41] K. Zhao, L. Xue, J. Liu, X. Gao, S. Wu, Y. Han, Y. Geng, *Langmuir* **2010**, *26*, 471.
[42] A. R. Aiyar, J. Hong, R. Nambiar, D. M. Collard, E. Reichmanis, *Adv. Funct. Mater.* **2011**, *21*, 2652.
[43] T. J. Prosa, M. J. Winokur, J. Moulton, P. Smith, A. J. Heeger, *Macromolecules* **1992**, *25*, 4364.
[44] S. Samitsu, T. Shimomura, S. Heike, T. Hashizume, K. Ito, *Macromolecules* **2008**, *41*, 8000.
[45] W. W. Graessley, S. F. Edwards, *Polymer* **1981**, *22*, 1329.
[46] B. O'Shaughnessy, *J. Chem. Phys.* **1991**, *94*, 1.
[47] B. Grévin, P. Rannou, R. Payerne, A. Pron, J. P. Travers, *J. Chem. Phys.* **2003**, *118*, 7097.
[48] J. Liu, R. S. Loewe, R. D. McCullough, *Macromolecules* **1999**, *32*, 5777.
[49] W. Hu, *Polymer Deformation*, Springer, Wien **2013**, pp. 93–125.
[50] J. E. Mark, *Physical Properties of Polymers Handbook*, Springer, New York **2007**, Ch. 25.
[51] S. L. Shenoya, W. D. Batesa, H. L. Frisch, G. E. Wnek, *Polymer* **2005**, *46*, 3372.
[52] F. P. V. Koch, J. Rivnay, S. Foster, C. Müller, J. Downing, E. Buchaca-Domingo, P. Westacott, L. Yu, M. Yuan, M. Baklar, Z. Fei, C. Luscombe, M. McLachlan, M. Heeney, G. Rumbles, C. Silva, A. Salleo, J. Nelson, P. Smith, N. Stingelin, unpublished.
[53] M. Koppe, C. J. Brabec, S. Heiml, A. Schausberger, W. Duffy, M. Heeney, I. McCulloch, *Macromolecules* **2009**, *42*, 4661.
[54] S. T. Turner, P. Pingel, R. Steyrleuthner, E. J. W. Crossland, S. Ludwigs, D. Neher, *Adv. Funct. Mater.* **2011**, *21*, 4640.
[55] J. Clark, C. Silva, R. H. Friend, F. C. Spano, *Phys. Rev. Lett.* **2007**, *98*, 206406.
[56] G. Louarn, M. Trznadel, J. P. Buisson, J. Laska, A. Pron, M. Lapkowski, S. Lefrant, *J. Phys. Chem.* **1996**, *100*, 12532.
[57] J. Gierschner, Y.-S. Huang, B. V. Averbeke, J. Cornil, R. H. Friend, D. Beljonne, *J. Chem. Phys.* **2009**, *130*, 044105.
[58] H. Sirringhaus, P. J. Brown, R. H. Friend, M. M. Nielsen, K. Bechgaard, B. M. W. Langeveld-Voss, A. J. H. Spiering, R. A. J. Janssen, E. W. Meijer, P. Herwig, D. M. de Leeuw, *Nature* **1999**, *401*, 685.
[59] A. Zen, J. Pflaum, S. Hirschmann, W. Zhuang, F. Jaiser, U. Asawapirom, J. P. Rabe, U. Scherf, D. Neher, *Adv. Funct. Mater.* **2004**, *14*, 757.
[60] M. Brinkmann, D. Aldakov, F. Chandezon, *Adv. Mater.* **2007**, *19*, 3819.
[61] M. Brinkmann, F. Chandezon, R. B. Pansu, C. Julien-Rabant, *Adv. Funct. Mater.* **2009**, *19*, 2759.
[62] C. Gammer, C. Mangler, C. Rentenberger, H. P. Karnthaler, *Scr. Mater.* **2010**, *63*, 312.
[63] V. Vohra, M. Campoy-Quiles, M. Garriga, H. Murata, *J. Mater. Chem.* **2012**, *22*, 20017.
[64] D. M. DeLongchamp, R. J. Kline, D. A. Fischer, L. J. Richter, M. F. Toney, *Adv. Mater.* **2011**, *23*, 319.
[65] K. E. Aasmundtveit, E. J. Samuelsen, M. Guldstein, C. Steinsland, O. Flornes, C. Fagermo, T. M. Seeberg, L. A. A. Pettersson, O. Inganäs, R. Feidenhans'l, S. Ferrer, *Macromolecules* **2000**, *33*, 3120.
[66] H. U. Khan, R. Li, Y. Ren, L. Chen, M. M. Payne, U. S. Bhansali, D.-M. Smilgies, J. E. Anthony, A. Amassian, *ACS Appl. Mater. Interfaces* **2013**, *5*, 2325.
[67] R. Li, H. U. Khan, M. M. Payne, D.-M. Smilgies, J. E. Anthony, A. Amassian, *Adv. Funct. Mater.* **2013**, *23*, 291.
[68] L. H. Jimison, S. Himmelberger, D. T. Duong, J. Rivnay, M. F. Toney, A. Salleo, *J. Polym. Sci., Part B: Polym. Phys.* **2013**, *51*, 611.
[69] S. D. D. V. Rughooputh, S. Hotta, A. J. Heeger, F. Wudl, *J. Polym. Sci., Part B: Polym. Phys.* **1987**, *25*, 1071.
[70] K. W. Chou, B. Yan, R. Li, E. Q. Li, K. Zhao, D. H. Anjum, S. Alvarez, R. Gassaway, A. Biocca, S. T. Thoroddsen, A. Hexemer, A. Amassian, *Adv. Mater.* **2013**, *25*, 1923.
[71] L. H. Jimison, M. F. Toney, I. McCulloch, M. Heeney, A. Salleo, *Adv. Mater.* **2009**, *21*, 1568.
[72] E. J. W. Crossland, K. Rahimi, G. Reiter, U. Steiner, S. Ludwigs, *Adv. Funct. Mater.* **2011**, *21*, 518.

© 2013 WILEY-VCH Verlag GmbH & Co. KGaA, Weinheim